Journal of Computational Physics 229 (2010) 2697–2718

Contents lists available at ScienceDirect

Journal of Computational Physics

journal homepage: www.elsevier.com/locate/jcp

# Shape and topology optimization based on the phase field method and sensitivity analysis

Akihiro Takezawa [a,*], Shinji Nishiwaki [b], Mitsuru Kitamura [a]

[a] Department of Social and Environmental Engineering, Hiroshima University, 1-4-1 Kagamiyama, Higashi-Hiroshima, Hiroshima, Japan
[b] Department of Mechanical Engineering and Science, Kyoto University, Yoshida Honmachi, Sakyo-ku, Kyoto, Japan

ARTICLE INFO

*Article history:*
Received 3 April 2009
Received in revised form 31 August 2009
Accepted 11 December 2009
Available online 21 December 2009

*Keywords:*
Shape optimization
Topology optimization
Phase field method
Sensitivity analysis
Level set method

ABSTRACT

This paper discusses a structural optimization method that optimizes shape and topology based on the phase field method. The proposed method has the same functional capabilities as a structural optimization method based on the level set method incorporating perimeter control functions. The advantage of the method is the simplicity of computation, since extra operations such as re-initialization of functions are not required. Structural shapes are represented by the phase field function defined in the design domain, and optimization of this function is performed by solving a time-dependent reaction diffusion equation. The artificial double well potential function used in the equation is derived from sensitivity analysis. The proposed method is applied to two-dimensional linear elastic and vibration optimization problems such as the minimum compliance problem, a compliant mechanism design problem and the eigenfrequency maximization problem. The numerical examples provided illustrate the convergence of the various objective functions and the effect that perimeter control has on the optimal configurations.



## 1. Introduction

The search for optimal structural shapes under various specified conditions is a very important, challenging and attractive subject for researchers. The field of structural optimization has a history spanning more than a century, and began with research on optimal truss layouts carried out by Michell [1]. Details of the history and methodologies of various proposed methods can be found in comprehensive reviews and textbooks [2–13]. We focus on shape optimization using boundary variation and topology optimizations. The key idea of shape optimization [7,10,11,13] is to update the shape of the boundary based on the shape sensitivity. Although this is a standard approach for structural optimization and enables many types of problems to be handled, it has the following fundamental drawbacks. The first shortcoming is the high computational cost of remeshing. Since the outline of the target structure is usually represented using a finite element mesh and the objective function and its sensitivity are numerically calculated using the finite element method, the mesh must be updated as the shape changes to maintain the accuracy of the analysis. The second drawback is the inability to provide for topological changes such as the nucleation or elimination of holes, which increases the likelihood of local optima.

Topology optimization [2,5,6,14], in contrast, does not have these drawbacks, since optimization is performed numerically using a fixed mesh and topological changes of the target structure are allowed. The basic idea is the replacement of the shape optimization problem by a two-phase material distribution problem consisting of an original material and an ersatz material mimicking voids. Unfortunately, these two-phase optimization problems do not have an optimal solution

* Corresponding author. Tel.: +81 82 424 7544; fax: +81 82 422 7194.
*E-mail addresses:* akihiro@hiroshima-u.ac.jp (A. Takezawa), shinji@prec.kyoto-u.ac.jp (S. Nishiwaki), kitamura@naoe.hiroshima-u.ac.jp (M. Kitamura).

0021-9991/$ - see front matter © 2009 Elsevier Inc. All rights reserved.
doi:10.1016/j.jcp.2009.12.017

unless smoothness or topological constraints are taken into account. To overcome this difficulty, a homogenization method is applied and the original problem is represented as a composite material optimization problem, namely, an optimization problem of a volume fraction of these materials. As a result, the optimal configurations obtained in topology optimization methods are represented as the distribution of a material density function. This representation raises the further problem of how to obtain clear shapes from the optimal density distribution without the use of filtering methods [15].

Recently, the level set method for structural optimization [16–19] have been proposed to avoid the drawbacks described above. In these methods, the target configuration is represented as a zero contour of the level set function and the function is updated based on the Hamilton–Jacobi equation. Level set methods allow topological changes (limited to the elimination of holes), significantly improving structural performance. Moreover, this method is free from remeshing, since the level set function is defined in an Eulerian coordinate system. The level set method was originally proposed by Osher and Sethian [20] as a numerical method for tracking free boundaries according to the mean curvature motion, and the mathematical background was subsequently clarified by several researchers [21–23]. It has been applied in many research fields, such as fluid mechanics and image processing, as a general free boundary tracking method. To achieve appropriate numerical accuracy, the level set method requires that the level set function be re-initialized during the update operation to maintain the signed distance characteristic of the function. The re-initialization operation is not an easy task, and although several approaches have been proposed (see [24–26] or Chapter 7 in [27]), this is a topic of ongoing research. In this paper, we focus on utilizing another free boundary tracking method, the phase field method, to avoid the need for re-initialization.

As with the level set method, the phase field method is capable of handling the motion caused by domain states such as temperature and the motion caused by the domain shape, such as the mean curvature motion, and so can also be applied to structural optimization. The phase field method was developed as a way to represent the surface dynamics of phase transition phenomena such as solid-liquid transitions. Research concerning such physical modeling can be traced back to Cahn and Hilliard [28] and Allen and Cahn [29]. The mathematical fundamentals for these physical models were constructed by several researchers [30–32]. In the early stage of this research, contributions concerning the computation of the actual phase transition phenomena were provided by Kobayashi [33] and Wang et al. [34]. The phase field method has been used in many surface dynamic simulations such as multi-phase flow [35] and crack-propagation [36] in addition to simulations of phase transition phenomena [37,38], and research where it is used as a general interface tracking method has also been reported recently [39]. Outlines of the above history and methodologies can be found in several comprehensive reviews [40–42].

The idea of applying the phase field method to structural optimization was first proposed by Bourdin and Chambolle [43,44], having initially been used to implement perimeter constraints [45,46]. The perimeter control effect of the phase field method makes it possible to obtain clear shapes free of gray scales or domain discontinuities, and a number of researchers have developed useful structural optimization methods that incorporate the phase field method [47–50]. It introduces an additional term into conventional topology optimization schemes, and the structural optimization is, for the most part, achieved using conventional topology optimization methodologies. Therefore, the nucleation of holes in the target structure can be achieved with these methods, whereas the phase field method itself does not allow the number of holes in the domain to be increased since it is a surface tracking method.

In contrast with the above methods, however, we develop a new intuitive phase field method for structural optimization. That is, the phase field method is used to represent the motion of optimized shape boundaries, much as the level set function does in the level set method for structural optimization. The structural shape is represented by the phase field function defined on the design domain containing the optimal configuration. The numerical computation is performed over the whole domain using a so-called ersatz material approach, as in conventional topology optimization. Optimization of the phase field function is achieved using a time-dependent reaction diffusion equation called the Allen–Cahn equation. An artificial double well potential used in the equation is derived from sensitivity analysis. That is, the difference between two minima of the potential is set based on the sensitivity analysis. The proposed optimization method is applied to the minimum compliance problem, a compliant mechanism design problem and the eigenfrequency maximization problem. The numerical examples provided illustrate the convergence of the objective function and optimal configurations, and the perimeter control effect is also discussed during the explanations. Our results indicate that the proposed method is as functional as the level set method for structural optimization, with simpler computation since it requires no re-initialization operation.

## 2. Phase field method

### 2.1. Phase field function and its evolutional equation

In this section, the phase field method is explained briefly. A phase field function $\phi(\boldsymbol{x})$ is defined over an entire analysis domain to represent the phase of the local points therein, as shown in Fig. 1. From a physical point of view, the phase field function provides the average phase of the local points. Consider a closed system composed of two phases, one of which corresponds to the value $\alpha$ of the phase field function while the other corresponds to the value $\beta$ ($\alpha < \beta$). The boundary of each phase is represented as a smooth function that interpolates the different values $\phi$, and is termed the "diffuse interface". The Van der Waals free energy of the system is given by

$$F(\phi) = \int_{\Omega} \left( \frac{\varepsilon}{2} |\nabla \phi|^2 + \varepsilon^{-1} f(\phi) \right) d\boldsymbol{x}, \tag{1}$$

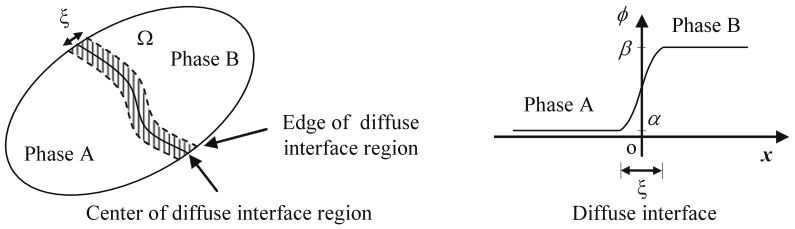


(a) A 2D domain represented by the phase field function

(b) A 1D illustration of the phase field function

**Fig. 1.** Examples of the phase field function.

where $\varepsilon > 0$ is a coefficient determining the effect of each term. The first term represents the interaction energy term of the field in mean field theory, and the second term represents a double well potential with the value $f'(\alpha) = f'(\beta) = 0$ as shown in Fig. 2. The double well potential indicates that there exist lower free energy values with minima corresponding to each phase.

Next, we introduce the time-dependent evolutional equation of the phase field function $\phi$. The change of the phase field function with respect to time is assumed to be linearly dependent upon the direction in which the free energy function is minimized:

$$\frac{\partial \phi}{\partial t} = -M(\phi)\frac{\delta F(\phi)}{\delta \phi}. \tag{2}$$

Substituting Eq. (1) into Eq. (2), the following equation can now be obtained:

$$\frac{\partial \phi}{\partial t} = M(\phi)(\varepsilon \nabla^2 \phi - \varepsilon^{-1} f'(\phi)). \tag{3}$$

Eq. (3) is known as the Allen–Cahn equation [29]. Below, several characteristics of the phase field method critical to our proposed method are explained.

### 2.2. Motion of the diffuse interface

The time-dependent motion of the diffuse interface in a domain represented by the phase field function $\phi(\boldsymbol{x})$ is governed by Eq. (3). The front moves in its normal direction at a speed determined by the difference between each minimum of the double well potential $f(\phi)$ and the curvature of the diffuse interface as follows:

$$v = s + \frac{1}{t}H + O\left(\frac{1}{t^2}\right), \quad t \gg 1, \tag{4}$$

where $s$ is the speed due to the difference between each minimum of the double well potential $f(\phi)$ and $H$ is the mean curvature of the diffuse interface. If the potential has equal minima, the motion is only governed by the mean curvature. Mathematical details and proofs of this are discussed in [51–53]. Here, we use the theory of the front motion governed by Eq. (3) for shape optimization. That is, the difference between each minimum of the double well potential $f(\phi)$ is determined by sensitivity analysis and the front of the optimized domain moves in a direction which reduces the value of the objective function, as discussed in the next section.

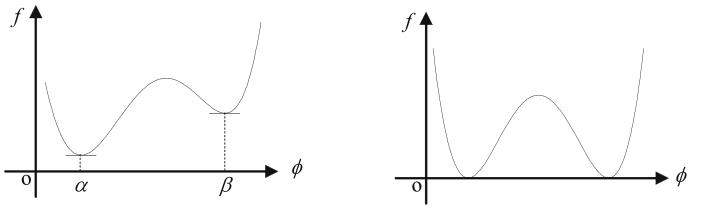


(a) An example of a double well potential

(b) The double well potential after affine translation

**Fig. 2.** Examples of a double well potential.

### 2.3. Perimeter minimization

Another important characteristic of the phase field method is the following problem of minimizing the total free energy represented by Eq. (1). The total volume of the phase field function is constrained to the value $V_\alpha$ and the double well function $f(\phi)$ has identical minima, that is, $f(\alpha) = f(\beta)$. The optimization problem is formulated as

$$\inf_{\substack{\phi \\ \int_\Omega \phi(\boldsymbol{x})dx = V_\alpha}} \int_\Omega \left(\frac{\varepsilon}{2}|\nabla\phi|^2 + \varepsilon^{-1} f(\phi)\right) dx, \tag{5}$$

the solution to which can be represented as

$$\phi_\varepsilon(\boldsymbol{x}) \approx \phi_{\alpha,\beta}(\boldsymbol{x}) + \phi_{\text{interface}}\left(\frac{\text{dist}(\boldsymbol{x}, S)}{\varepsilon}\right). \tag{6}$$

The phase field function $\phi_{\alpha,\beta}$ takes the values $\alpha$ or $\beta$ with a minimum boundary $S$ in the domain $(\boldsymbol{x} \in \Omega | \phi(\boldsymbol{x}) = \alpha)$, and $\phi_{\text{interface}}$ is a function that tends to zero at infinity, giving a diffuse interface domain between these phases. That is, $\lim_{x\to\infty} \phi_{\text{interface}}(x) = 0$, representing diffuse interfaces. Also, $\text{dist}(\boldsymbol{x}, S)$ is the distance function from the boundary $S$. The results can be explained as the interaction between the first term of Eq. (5), penalizing unnecessary diffuse interfaces, and the second term that approaches the value of $\alpha$ or $\beta$. Thus, when $\varepsilon \to 0$, Eq. (5) can be approximated as a minimal perimeter problem as follows:

$$\inf_{\substack{\phi \\ \int_\Omega \phi(\boldsymbol{x})dx = V_\alpha}} \quad \text{Per}((\boldsymbol{x} \in \Omega | \phi(\boldsymbol{x}) = \alpha)), \tag{7}$$

where $\text{Per}(A)$ denotes the perimeter of domain $A$. Note that the above formulation can be applied to general double well functions that have non-identical minima by applying an affine translation as shown in Fig. 2. In this case, the function converges to an optima under the driving force caused by the difference between the minima and perimeter minimization. Mathematical details and proofs can be found in [54,55].

Note that some methods have been proposed which apply the theory of perimeter minimization characteristic of the phase field method to perimeter control of topology optimization methods. Bourdin and Chambolle [43,44] first proposed a phase field method-based topology optimization problem for a structure with design-dependent loading. They proposed the following new objective function, using Eq. (5) to penalize the original objective function $F$ under the assumption that $\varepsilon \to 0$:

$$\inf_{\substack{\rho \\ \int_\Omega \rho(\boldsymbol{x})dx = V_0}} \quad F(\rho) + \gamma P_\varepsilon(\rho), \tag{8}$$

where

$$P_\varepsilon(\rho) = \int_\Omega \left(\frac{\varepsilon}{2}|\nabla\phi|^2 + \varepsilon^{-1} f(\rho)\right) dx, \tag{9}$$

where $\rho$ is the function representing the local density in topology optimization and $\gamma$ is a Lagrange multiplier for the perimeter term $P_\varepsilon$. As mentioned above, when $\varepsilon \to 0$, $P_\varepsilon$ forces the function $\rho$ to converge to $\{0,1\}$ and the resulting domain $(\boldsymbol{x} \in \Omega | \rho(\boldsymbol{x}) = 1)$ to have minimal perimeter. Thus, the method is useful for approximating the original topology optimization, which is two-phase material distribution optimization problem [47]. Similar types of topology optimization methods were also developed by Wang and Zhou [48–50] and Burger [47]. The Cahn–Hilliard equation [28], a time-dependent evolutional equation representing the volume of the conserved field, is used to update the phase field function in [49,50]. This facilitates the handling of volume constraints, in contrast to other time-dependent PDE-based structural optimization methods.

We remark that the primary difference between these methods and our method is in their origin. Since the methods above came from topology optimization, which updates the density function based on sensitivity analysis, the nucleation of holes in the target structure is possible. On the other hand, our method aims for the same outcome using the level set method for shape optimization, whose roots are in classical shape optimization based on boundary variation. Thus, there are no hole nucleation mechanisms in our method. Despite the common name "phase field method", the two approaches have different backgrounds and functions. Of course, their effectiveness depends on the application.

## 3. Formulation

### 3.1. Setting of original problem

As the first step towards constructing a shape optimization method based on the phase field method, we define a particular shape optimization problem. Let $\Omega$ be the domain that varies during the optimization process, with the state of $\Omega$ represented by some partial differential equations. The boundary $\partial\Omega$ of $\Omega$ is divided into two boundaries, a boundary $\partial\Omega_D$ with

Dirichlet boundary conditions and a boundary $\partial\Omega_N$ with Neumann boundary conditions. The state variable $\boldsymbol{u}$ is calculated based on the state equations that have these boundary conditions. We introduce the extended design domain $D$ that contains $\Omega$. Here, a set of admissible shapes with fixed volume $V_0$ in $D$ can be represented as follows:

$$\mathcal{U}_{ad} = \{\Omega \subset D | \Omega \in \mathbb{R}^d,\ |\Omega| = V_0\}. \tag{10}$$

Thus, the shape optimization problem for $\Omega$ is defined as

$$\inf_{\Omega \in \mathcal{U}_{ad}} J(\Omega), \tag{11}$$

where $J(\Omega)$ is a functional with respect to state variable $\boldsymbol{u}$ whose value depends on the shape of $\Omega$. This is a typical shape optimization problem, and a new numerical method for its solution is explained in this paper. We call this "shape and topology optimization", since the optimization is performed by varying boundaries as well as through typical shape optimization methods [11,13], and changes in topology are allowed as in topology optimizations [5,14]. The proposed method, in some sense, functions in a way that resembles the level set method for structural optimization [16,19].

### 3.2. Domain representation by the phase field function

We represent the shapes of optimized domains using a phase field function as shown in Fig. 3. The phase field function $\phi(\boldsymbol{x})$ $(0 \leqslant \phi \leqslant 1)$ is defined in the domain $D$. We consider a setting where the domain $\Omega_1$ $(\boldsymbol{x} \in D | \phi(\boldsymbol{x}) = 1)$ corresponds to the optimized shape $\Omega$ and the domain $\Omega_0$ $(\boldsymbol{x} \in D | \phi(\boldsymbol{x}) = 0)$ corresponds to $D \setminus \Omega$. However, this setting is insufficient because a diffuse interface region exists when the phase field method is used, as explained in Section 2. Let $\xi$ represent the diffuse interface region. The domain representation of $D$ is then formulated as

$$\begin{aligned} &\phi = 1 \Longleftrightarrow \boldsymbol{x} \in \Omega_1, \\ &0 < \phi < 1 \Longleftrightarrow \boldsymbol{x} \in \xi, \\ &\phi = 0 \Longleftrightarrow \boldsymbol{x} \in \Omega_0, \end{aligned} \tag{12}$$

where

$$(\Omega_1 \cup \xi) \supset \Omega \quad \text{and} \quad (\Omega_0 \cup \xi) \supset D \setminus \Omega. \tag{13}$$

That is, the original domain $\Omega$ is represented as a subset of the union of $\Omega_1$ and $\xi$. In the above setting, the position of the boundary $\partial\Omega$ is unclear except that it lies in $\xi$. However, as explained in Section 2, the diffuse interface region becomes very thin when $\varepsilon$ is very small, in which case $\xi$ can be regarded as approximately representing $\partial\Omega$. Actually, numerical examples show that almost clear shapes with very thin boundaries can be obtained by our method. A clear shape can be easily picked out in a plot by choosing an arbitrary contour value such as $\phi = 0.5$ in the diffuse interface.

### 3.3. Problem details

Consider the linear elastic problem in the above domain represented by the phase field function. The elasticity equations for state $\boldsymbol{u}$ are defined over the entire domain $D$ using the ersatz material approach. In this approach, $\Omega_1$ is filled with a material whose elasticity tensor is $\boldsymbol{A}$ and $\Omega_0$ is assumed to be filled with a material that mimics a void to avoid singularities in the stiffness matrix. In addition, the material in the diffuse interface $\xi$ must be defined, but the state of this domain is unclear except that it is in transition from the conditions of $\Omega_0$ and $\Omega_1$. We set a virtual physical property $\boldsymbol{A}^*$ of the entire domain using an interpolation function $k(\phi)$ defined in the range $k_{\min} \leqslant k(\phi) < 1$:

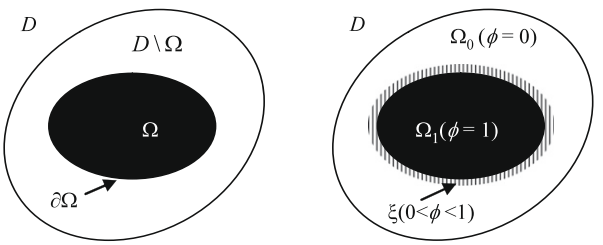


(a) An original domain (b) The domain represented by the phase field function

**Fig. 3.** The domain representation by the phase field function.

$$\boldsymbol{A}^*(\phi) = \begin{cases} \boldsymbol{A} & \text{if } \boldsymbol{x} \in \Omega_1, \\ k(\phi)\boldsymbol{A} \ (k_{\min} \leqslant k(\phi) < 1) & \text{if } \boldsymbol{x} \in \xi, \\ k_{\min}\boldsymbol{A} & \text{if } \boldsymbol{x} \in \Omega_0, \end{cases} \tag{14}$$

where

$$A_{ijkl} = \lambda\delta_{ij}\delta_{kl} + \mu(\delta_{ik}\delta_{jl} + \delta_{il}\delta_{jk}), \tag{15}$$

$$\lambda = \frac{v}{(1+v)(1-2v)}E, \quad \mu = \frac{1}{2(1+v)}E. \tag{16}$$

The term $A_{ijkl}$ denotes the components of the elasticity tensor $\boldsymbol{A}$, $\delta$ denotes the Kronecker delta, $\lambda$ and $\mu$ are Lamé moduli, $E$ is the Young modulus and $v$ is the Poisson ratio of the material. Note that this formulation is somewhat similar to that of the SIMP method [56], a well-known interpolation scheme used in topology optimization methods, in that the virtual material property is defined for intermediate values of the function representing the material state. However, the physical meanings are quite different. While the density function of the SIMP method can be the regarded as the weak convergence limit of a characteristic function based on homogenization theory, the phase field function $\phi$ in our method is just a numerical interpolation. Homogenization theory cannot be applied to problems that penalize properties of the boundary such as gradient and diffusion [57].

Let the boundary $\partial D$ of the extended design domain $D$ be composed of the following three parts: $\partial D_{\mathrm{D}}$ with Dirichlet boundary conditions, $\partial D_{\mathrm{N}}$ with non-homogeneous Neumann boundary conditions having surface loads $\boldsymbol{g} \neq \boldsymbol{0}$, and $\partial D_{\mathrm{N0}}$ with traction-free Neumann boundary conditions. These boundary conditions correspond to the boundary conditions of the original domain $\Omega$ as follows:

$$\partial\Omega_{\mathrm{D}} \subset \partial D_{\mathrm{D}}, \quad \partial\Omega_{\mathrm{N}} = \partial D_{\mathrm{N}} \cup \partial\Omega_{\mathrm{N0}}, \tag{17}$$

where $\partial\Omega_{\mathrm{N0}}$ is the boundary of the original domain and the domain with traction-free Neumann boundary conditions. Surface loads are applied on the fixed boundary $\partial\Omega_{\mathrm{N}}$ during the optimization process, and the other boundaries are regarded as traction-free. We let $\boldsymbol{g}$ be the surface load vector and assume that volume forces are ignored. The following weak form state equation is then formulated for state variable $\boldsymbol{u}$:

$$\int_D \boldsymbol{A}^*(\phi)\boldsymbol{e}(\boldsymbol{u}) : \boldsymbol{e}(\boldsymbol{v})dx = \int_{\partial D_{\mathrm{N}}} \boldsymbol{g}\cdot\boldsymbol{v}ds, \quad \text{for } \boldsymbol{u} \in V, \ \forall \boldsymbol{v} \in V, \tag{18}$$

$$V = \{\boldsymbol{v} \in H^1(\Omega)^N | \boldsymbol{v} = 0 \quad \text{on } \Gamma_D\}, \tag{19}$$

$$\boldsymbol{e}(\boldsymbol{u}) = \frac{1}{2}(\nabla\boldsymbol{u} + (\nabla\boldsymbol{u})^T), \tag{20}$$

where $\boldsymbol{v}$ is the test function, $\boldsymbol{e}$ is the strain tensor and $H^1$ is a Sobolev space.

For the above linear elastic problem, the compliance minimization problem, which is the most basic structural optimization problem, is considered first. The compliance, equal to the work done by the load, is

$$J_1(\phi) = \int_{\partial D_{\mathrm{N}}} \boldsymbol{g}\cdot\boldsymbol{u}ds. \tag{21}$$

The least square error compared with the target displacement is also considered, represented as

$$J_2(\phi) = \left(\int_D c(\boldsymbol{x})|\boldsymbol{u} - \boldsymbol{u}_0|^\alpha dx\right)^{1/\alpha}, \tag{22}$$

where $c(\boldsymbol{x})$ is a coefficient function denoting the location of the target displacement and $\boldsymbol{u}_0$ is the target displacement vector. This objective function is in design optimizations of compliant mechanisms [58,59].

We also consider a vibration optimization problem for a linear elastic domain, which requires us to define the mass density function $\rho^*$ in $D$. As for the case where an elasticity tensor is used, $\Omega_1$ is filled with a material with mass density $\rho$ and $\Omega_0$ is assumed to be filled with a very light material. The mass density function in the domain $\xi$ is defined as the product of the original mass density with an interpolation function $m(\phi)$ in the range $m_{\min} \leqslant m(\phi) < 1$:

$$\rho^*(\phi) = \begin{cases} \rho & \text{if } \boldsymbol{x} \in \Omega_1, \\ m(\phi)\rho \ (m_{\min} \leqslant m(\phi) < 1) & \text{if } \boldsymbol{x} \in \xi, \\ m_{\min}\rho & \text{if } \boldsymbol{x} \in \Omega_0. \end{cases} \tag{23}$$

The vibration frequencies and the modes are computed using the following eigenvalue problem, which is represented in weak form:

$$\int_D \boldsymbol{A}^*(\phi)\boldsymbol{e}(\boldsymbol{u}_k) : \boldsymbol{e}(\boldsymbol{v})dx = \omega_k^2 \int_D \rho^*(\phi)\boldsymbol{u}_k\cdot\boldsymbol{v}dx, \quad \text{for } \boldsymbol{u}_k \in V, \ \forall \boldsymbol{v} \in V, \tag{24}$$

where $\omega_k$ is the $k$th eigenfrequency and $\boldsymbol{u}_k$ is the $k$th eigenmode vector. The objective function is the weighted summation of the squares of the eigenfrequencies:

$$J_3(\phi) = -\sum_{k=1}^{n} w_k \omega_k^2 = -\sum_{k=1}^{n} w_k \lambda_k, \tag{25}$$

where $\lambda_k$ is the $k$th eigenvalue obtained by

$$\omega_k^2 = \lambda_k = \min_{\boldsymbol{u}_1,\ldots,\boldsymbol{u}_k \in V} \max_{\boldsymbol{u} \in \mathrm{span}[\boldsymbol{u}_1,\ldots,\boldsymbol{u}_k]} \frac{\int_D \boldsymbol{A}^*(\phi)\boldsymbol{e}(\boldsymbol{u}) : \boldsymbol{e}(\boldsymbol{u}) dx}{\int_D \rho^*(\phi)|\boldsymbol{u}|^2 dx}. \tag{26}$$

The volume constraint is imposed using a Lagrange multiplier method, and the objective function is reformulated as

$$\min_{\phi} \bar{J}(\phi) = \min_{\phi} \left( J_1(\phi), J_2(\phi) \text{ or } J_3(\phi) + \zeta \int_D \phi dx \right), \tag{27}$$

where $\zeta$ is the positive Lagrange multiplier.

### 3.4. Evolution of the phase field function

The phase field function evolves with a virtual time $t$ in the interval $t_1 \leqslant t \leqslant t_2$, corresponding to a descent step of the function in the optimization problem. The evolutional equation is formulated as

$$\begin{cases} \frac{\partial \phi}{\partial t} = \kappa \nabla^2 \phi - f'(\phi) \quad (t_1 \leqslant t \leqslant t_2), \\ \frac{\partial \phi}{\partial \boldsymbol{n}} = 0 \quad \text{on } \partial D, \end{cases} \tag{28}$$

where $\kappa$ is a positive coefficient of the diffusion term and $f(\phi)$ is a double well potential. As explained in Section 2, when the phase field function follows Eq. (28), the diffuse interface of the domain represented by the phase field function moves in a normal direction. The velocity is determined by the difference between the minima of the double well potential and the mean curvature of the diffuse interface. The difference between the minima of the double well potential gives the velocity from the larger minimum to the smaller minimum. To move the diffuse interface in the direction in which the objective function decreases, we set the double well potential $f(\phi)$ to satisfy the following conditions:

$$f(0) = 0, \quad f(1) = h\bar{J}'(\phi_{t_1}), \quad f'(0) = f'(1) = 0 \quad (h > 0), \tag{29}$$

where $J'(\phi)$ is the sensitivity of the objective function with respect to $\phi$, $\phi_{t_1}$ is the value of $\phi$ at time $t_1$ and $h$ is its positive coefficient. That is, we determine the difference between potential minima based on sensitivity analysis. A sketch of the double well potential is shown in Fig. 4. Since the function evolves in the direction of the smaller minimum of the double well potential, the phase field function at time $t_2$ for $\boldsymbol{x} \in \xi$ is approximately represented as

$$\phi_{t_2}(\boldsymbol{x}) \approx \phi_{t_1}(\boldsymbol{x}) - a(t_1)\bar{J}'(\phi_{t_1}), \tag{30}$$

where $a(t)$ is positive and represents the rate of change of $\phi$. Eq. (30) can also be regarded as the evolution of the design variable $\phi$ based on the steepest descent method with descent step $a(t_1)$. That is, the minimization of the objective function can be achieved in the same way as for conventional steepest descent methods.

### 3.5. Perimeter constraints

We return now to the derivation of Eq. (28). The equation is derived under the assumption that the total free energy, given by

$$\int_D \left( \frac{\kappa}{2} |\nabla \phi|^2 + f(\phi) \right) dx, \tag{31}$$

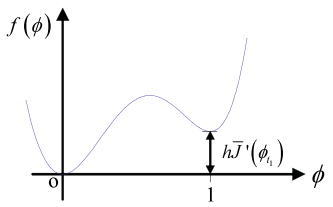


**Fig. 4.** Sketches of the double well potential.

decreases linearly as explained in Section 2. When $\kappa$ is very small and the total volume of the phase field function is constrained, the minimization problem of the free energy can be also regarded as a perimeter minimization problem on $\Omega_1$ ($\boldsymbol{x} \in D | \phi(\boldsymbol{x}) = 1$). We regard $\phi$ to be a non-conservative function and update it using an Allen–Cahn equation. Since the volume constraint is included in the objective function as shown in Eq. (27), the total volume of the phase field function is constrained to a fixed value in a converged optimal solution, although the total volume cannot be completely preserved during optimization. Thus, the perimeter minimization effect included in the minimization problem of free energy in Eq. (31) must also be considered. Numerical examples provided later show the effect of perimeter control upon the optimal shape for different values of $\kappa$.

### 3.6. Sensitivity analysis

The double well potential $f(\phi)$ requires sensitivity analysis of the objective function with respect to $\phi$. Since the function is defined on $D$ and the optimization problem is a domain state variation problem, its sensitivity analysis closely resembles the topology optimization method and the derivations are well known. Thus, only the results are shown here and the detailed derivation is explained in Appendix A.

The sensitivity of the compliance in Eq. (21) is given by

$$J_1'(\phi) = -\boldsymbol{A}^{*\prime}(\phi)\boldsymbol{e}(\boldsymbol{u}) : \boldsymbol{e}(\boldsymbol{u}). \tag{32}$$

The sensitivity of the least square error compared with the target displacement from Eq. (22) is

$$J_2'(\phi) = \boldsymbol{A}^{*\prime}(\phi)\boldsymbol{e}(\boldsymbol{u}) : \boldsymbol{e}(\boldsymbol{p}), \tag{33}$$

where $\boldsymbol{p}$ is an adjoint state vector which satisfies following equation:

$$\int_D \boldsymbol{A}^*(\phi)\boldsymbol{e}(\boldsymbol{p}) : \boldsymbol{e}(\boldsymbol{q})dx + C_0 c(\boldsymbol{x})|\boldsymbol{u} - \boldsymbol{u}_0|^{\alpha-2}(\boldsymbol{u} - \boldsymbol{u}_0)\boldsymbol{q} = 0, \quad \text{for } \boldsymbol{p} \in V, \ \forall \boldsymbol{q} \in V, \tag{34}$$

where

$$C_0 = \left( \int_D c(\boldsymbol{x})|\boldsymbol{u} - \boldsymbol{u}_0|^{\alpha} dx \right)^{1/\alpha - 1}. \tag{35}$$

The sensitivity of the weighted summation of eigenvalues in Eq. (25) is

$$J_3'(\phi) = -\sum_{k=1}^{n} w_k \lambda_k'(\phi), \tag{36}$$

where

$$\lambda_k'(\phi) = \boldsymbol{A}^{*\prime}(\phi)\boldsymbol{e}(\boldsymbol{u}_k) : \boldsymbol{e}(\boldsymbol{u}_k) - \lambda_k \rho^{*\prime}(\phi)|\boldsymbol{u}_k|^2. \tag{37}$$

## 4. Numerical implementation

### 4.1. Setting of evolutional equation

Since the double well potential must satisfy Eq. (29), we set it to be

$$f(\phi) = W(\boldsymbol{x})w(\phi) + G(\boldsymbol{x})g(\phi), \tag{38}$$

where

$$w(\phi) = \phi^2(1 - \phi^2), \quad g(\phi) = \phi^3(6\phi^2 - 15\phi + 10), \tag{39}$$

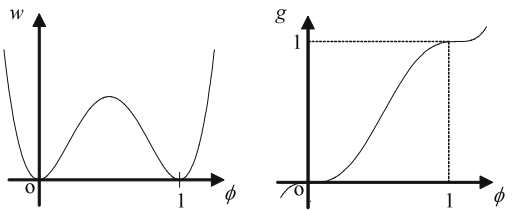


(a) Function $w$ (b) Function $g$

**Fig. 5.** Sketches of function $w$ and $g$.

which are the same as those used in [38]. $w(\phi)$ is a function such that $w(0) = w(1) = w'(0) = w'(1) = 0$, and $g(\phi)$ is a function such that $g(0) = 0,\ g(1) = 1$ and $g'(0) = g'(1) = 0$. Sketches of these functions are shown in Fig. 5. $W(\boldsymbol{x})$ and $G(\boldsymbol{x})$ are coefficients of these functions. The advantage of these choices for $w(\phi)$ and $g(\phi)$ is that the double well characteristic of $f(\phi)$ in Eq. (29) can be kept for any $W(\boldsymbol{x})$ and $G(\boldsymbol{x})$. $W(\boldsymbol{x})$ determines the height of the wall of the double well potential, which affects the thickness of the diffuse interface. $W(\boldsymbol{x})$ is set to be $\frac{1}{4}$ here. In the phase transition simulation, the coefficient is usually decided in relation to the latent heat of the material. Since the phase field method is used here as a free surface tracking method without any physical background, the value chosen is simple. (As a result, the coefficient of the highest order term $\phi^3$ of $W(\boldsymbol{x})w'(\phi)$ is 1.) The value of $G(\boldsymbol{x})$ is chosen to be $G(\boldsymbol{x}) = h\bar{J}'(\phi_{t_1})$, which is composed of the sensitivity $\bar{J}'(\phi)$ and the coefficient $h$ used in Eq. (29). Since the order of $\bar{J}'(\phi)$ depends on the optimization problem, the appropriate value of $h$ must be adjusted in each case. To avoid such complicated parameter settings, we first normalize the sensitivity by dividing by its $L^2$-norm, and the new coefficient $\eta$ is set as follows:

$$G(\boldsymbol{x}) = \eta \frac{J'(\phi_{t_1})}{\|J'(\phi_{t_1})\|}. \tag{40}$$

Substituting Eqs. (38)–(40) into Eq. (28), we obtain

$$\begin{aligned}\frac{\partial \phi}{\partial t} &= \kappa \nabla^2 \phi - \frac{\partial}{\partial \phi}(W(\boldsymbol{x})w(\phi) + G(\boldsymbol{x})g(\phi)) = \kappa \nabla^2 \phi - \left(\frac{1}{4}w'(\phi) + \eta \frac{J'(\phi_{t_1})}{\|J'(\phi_{t_1})\|}g'(\phi)\right) \\ &= \kappa \nabla^2 \phi + \phi(1-\phi)\left\{\phi - \frac{1}{2} - 30\eta \frac{J'(\phi_{t_1})}{\|J'(\phi_{t_1})\|}(1-\phi)\phi\right\} \quad (t_1 \leqslant t \leqslant t_2).\end{aligned} \tag{41}$$

### 4.2. Setting of physical property

The material property functions $k(\phi)$ and $m(\phi)$ with respect to the elasticity tensor and mass in the diffuse interface domains are

$$k(\phi) = \min(\phi^p, k_{\min}), \quad m(\phi) = \min(\phi, m_{\min}), \tag{42}$$

where $p$ is a positive constant. We employ the interpolation function used in the SIMP method for the topology optimization [5,56]. The optimization was run using a variety of settings, and since those above yielded the best performance, we will use them in all of our numerical examples.

### 4.3. Algorithm

Based on the above formulation, the optimization algorithm is constructed as follows:

1. Set the initial value of phase field function $\phi$ expressing the initial shape of domain $\Omega$.
2. Iterate the following procedure until convergence:
   (a) Calculate the state variable $\boldsymbol{u}$ and adjoint state $\boldsymbol{p}$ with respect to $\phi_n$ at $n$th iteration by solving the state equation shown in Eq. (18) or Eq. (24) using the finite element method.
   (b) Calculate the objective function in Eq. (27).
   (c) Calculate the sensitivity of the objective function in Eqs. (32), (33) or Eq. (36) and prepare the evolutional equation for $\phi$ in Eq. (41).
   (d) Calculate the updated value of $\phi$ by solving Eq. (41).
3. Obtain the optimal shape of $\Omega$ expressed as the optimal distribution of $\phi$. (For example, the 0.5 level set of $\phi$ can be used as a criterion.)

### 4.4. Numerical method for the evolutional equation

The finite difference method is used to solve Eq. (41) numerically. Let us consider the case that the equation is solved by an explicit scheme. Because of the diffusion term, the time step $\Delta t$ is restricted by the following CFL condition for stable convergence in the 2D case:

$$\kappa\left(\frac{\Delta t}{(\Delta x)^2} + \frac{\Delta t}{(\Delta y)^2}\right) \leqslant \frac{1}{2}, \tag{43}$$

where $\Delta t > 0$ is the time step and $\Delta x$ and $\Delta y$ are space steps in the $x$ and $y$ directions, respectively. In general phase field methods, including our method, the coefficients of the diffusion terms are set to very small values over $\Delta x$. Thus, a relatively

large value can be chosen for $\Delta t$ even if an explicit scheme is used. However, even if the CFL condition is satisfied, the time step can take only very small values due to the reaction term. This term makes the function $\phi$ diverge once its value is outside the interval $0 \leqslant \phi \leqslant 1$. To avoid this problem, the reaction term is discretized by a so-called semi-implicit scheme [38] in which forward time terms are partly included. In the 2D case, let $\phi_{ij}^n$ be the value of $\phi$ at the $n$th iteration at the point $\boldsymbol{x}_{ij}$. The scheme then leads to the following discretization:

$$\frac{\phi_{ij}^{n+1}-\phi_{ij}^{n}}{\Delta t}=\kappa\left(\frac{\phi_{i-1,j}^{n}-2\phi_{ij}^{n}+\phi_{i+1,j}^{n}}{(\Delta x)^2}+\frac{\phi_{i,j-1}^{n}-2\phi_{ij}^{n}+\phi_{i,j+1}^{n}}{(\Delta y)^2}\right)+\begin{cases}\phi_{ij}^{n+1}\left(1-\phi_{ij}^{n}\right)r\left(\phi_{ij}^{n}\right) & \text{for } r\left(\phi_{ij}^{n}\right)\leqslant 0,\\ \phi_{ij}^{n}\left(1-\phi_{ij}^{n+1}\right)r\left(\phi_{ij}^{n}\right) & \text{for } r\left(\phi_{ij}^{n}\right)>0,\end{cases} \tag{44}$$

where

$$r\left(\phi_{i,j}^{n}\right)=\phi_{i,j}^{n}-\frac{1}{2}-30\eta\frac{J'(\phi_{t_1})}{\|J'(\phi_{t_1})\|}\phi_{i,j}^{n}\left(1-\phi_{i,j}^{n}\right). \tag{45}$$

As detailed in Appendix B, the above discretization guarantees that $\phi$ remains in the interval $0 \leqslant \phi \leqslant 1$ even when the time step is large. Although the forward time term $\phi^{n+1}$ is included in the right-hand side of the above equation, $\phi^{n+1}$ can obviously be calculated easily without solving a linear system, and the computational cost is almost equal to that for the ordinal explicit scheme.

The time step can be regarded as a descent step in the steepest descent method. Thus, for fast convergence, the value of the time step should be large enough to maintain decreasing values of the objective function. Since the time step is limited by the CFL condition in Eq. (43), we perform several calculations to update $\phi$ in Eq. (44) for each FEM. In numerical examples, the number of updates is automatically adjusted to keep the objective function decreasing.

All but one of the numerical examples explained later are calculated using the above finite difference method on structured quadrangular meshes. The other example is performed on an unstructured triangular mesh to check the mesh dependency of our method. In that case, the finite volume method [60] with semi-implicit discretization is used to solve Eq. (41).

### 4.5. Treatment of volume constraints

To limit the total volume of an optimal configuration, a total volume of the phase field function is added to the objective function as shown in Eq. (27). However, in this formulation, the relationship between the value of the Lagrange multiplier $\zeta$ and a converged total volume of a optimal configuration is unclear and depends on $\bar{J}(\phi)$. Thus, to fix the volume of the optimal configuration to a specified value, we update the Lagrange multiplier $\zeta^n$ at the $n$th iteration using the following equation, as in [61]:

$$\zeta^{n+1}=0.5\left(\zeta^n+\frac{\int_\xi j(\phi^n)dx}{\int_\xi \phi^n dx}\right)+\varepsilon_\zeta\left(\int_D \phi^n dx-V_0\right), \tag{46}$$

where $\int_D j(\phi)dx = J_1(\phi)$, $J_2(\phi)$ or $J_3(\phi)$, $V_0$ is a specified volume and $\varepsilon_\zeta > 0$ is a positive parameter.

## 5. Numerical example

The following numerical examples are provided to confirm the utility of the proposed method. In all examples, a virtual material with the normalized Young modulus $E$ of 1.0 and Poisson ratio $\nu$ of 0.3 is assumed. The values $k_{\min}$ and $m_{\min}$ in Eqs. (14) and (23) are set to $10^{-5}$ and $10^{-3}$, respectively. The penalization parameter $p$ in Eq. (42) is set to 3. The coefficient of normalized sensitivity $\eta$ in Eq. (41) is set to 20. Except for in specified cases, a quadrangular mesh is used for discretizations of both the phase field function and the displacement. At each iteration, we perform a finite element analysis of the state equation and 20 updates of the evolutional equation for the phase field function by solving the finite difference equation of the semi-implicit scheme. The number of updates is automatically decreased if the objective function does not decrease. The time step $\Delta t$ of the process is set to be half the Courant number. In the finite element analysis, isoparametric elements are used. All optimal configurations are plotted as the distribution of the phase field function of the optimal results.

### 5.1. 2D cantilever example

As a benchmark problem for the proposed method, stiffness maximization of a cantilever is performed, as illustrated in Fig. 6(a). The design domain is a $2 \times 1$ rectangle with a fixed boundary condition on the left side and a unit vertical point load at the center of the right side. The minimized objective function is formulated as the combination of the compliance represented in Eq. (21) and the total volume of the structure. The domain is discretized with a $200 \times 100$ rectangular mesh and the value of the Lagrange multiplier $\zeta$ is fixed at 80 during the optimization process. We set $\kappa = 1 \times 10^{-5}$ in Eq. (41).

Given the initial shape as shown in Fig. 6(b), Fig. 7 shows a configuration obtained after only 10 iterations and the optimal configuration obtained after 40 iterations. These figures show that the proposed method can affect topological changes only in the form of decreasing the number of holes, but lacks a hole nucleation mechanism. Approximately 40 iterations were

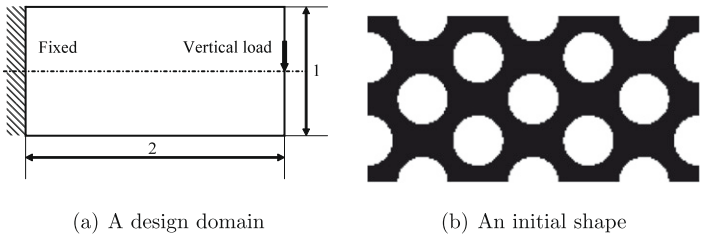


(a) A design domain (b) An initial shape

**Fig. 6.** A design domain and an initial shape for the cantilever example.

(a) Iteration 10 (b) Iteration 40

**Fig. 7.** Optimal configurations of the cantilever example on a $200 \times 100$ mesh at iterations 10 and 40.

required for convergence, and the objective function history is shown in Fig. 8. The resulting optimal configuration and required number of iterations are reasonable compared with other structural optimization methods such as [5,16]. The stationary values of the objective function during the first and second iteration are peculiar characteristics. Since there are no diffuse interfaces in the initial shape, the optimization at the first iteration is dominated by pure diffusion, without any effect from updating using sensitivities. From the second iteration, the diffuse interfaces that have been generated move in their normal directions according to the sensitivity analysis.

Next, the same problem is solved using a differently sized mesh to confirm the robustness of the proposed method with respect to mesh discretization. Fig. 9 shows a configuration obtained after only five iterations, and the optimal configuration obtained after 20 iterations, using $100 \times 50$ quadratic elements. The initial shape and parameters are the same as before

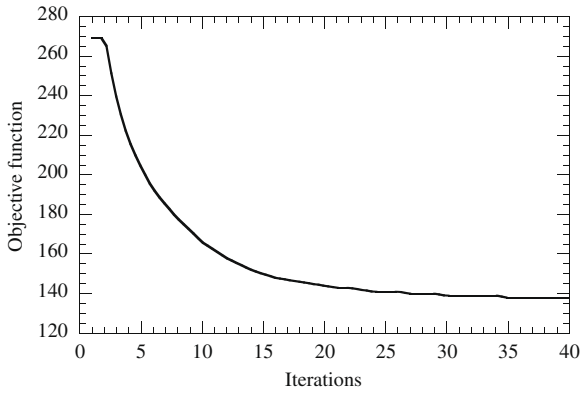


**Fig. 8.** The convergence history of the objective function of the cantilever example.

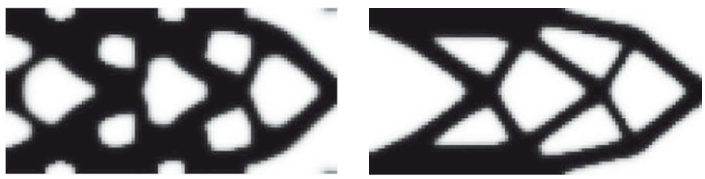

(a) Iteration 5 (b) Iteration 20

**Fig. 9.** Optimal configurations of the cantilever example on a coarser $100 \times 50$ mesh at iterations 5 and 20.

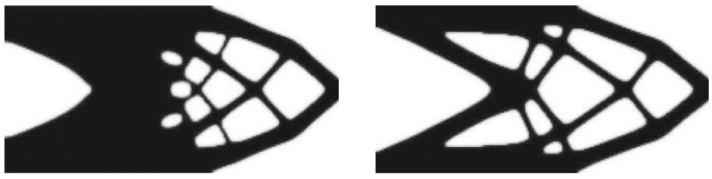

(a) Iteration 25 (b) Iteration 50

**Fig. 12.** Optimal configurations of the cantilever example with topological derivative at iterations 25 and 50.

### 5.3. 3D cantilever example

Finally, an optimization of a simple 3D cantilever shown in Fig. 13(a) is performed. The domain is discretized with a $60 \times 24 \times 30$ cubic mesh and the value of the Lagrange multiplier $\zeta$ is updated to adjust the total volume of the optimal configuration to 0.55 (20% of total volume) during the optimization process. Only half of the domain is computed due to symmetry. We set $\kappa = 1.5 \times 10^{-4}$ in Eq. (41). The first 40 iterations are performed with this setting, and the last 10 iterations are performed with the value $\kappa$ decreased to $5 \times 10^{-6}$ to obtain a thin interface domain. Fig. 14 shows the $\phi = 0.1$, 0.5 and 0.9 isosurfaces after the 50 iterations with the initial shape shown in Fig. 13(b). Although the thickness of the interface domain is not negligible, almost the same shape and topology can be picked out from any of the isosurfaces.

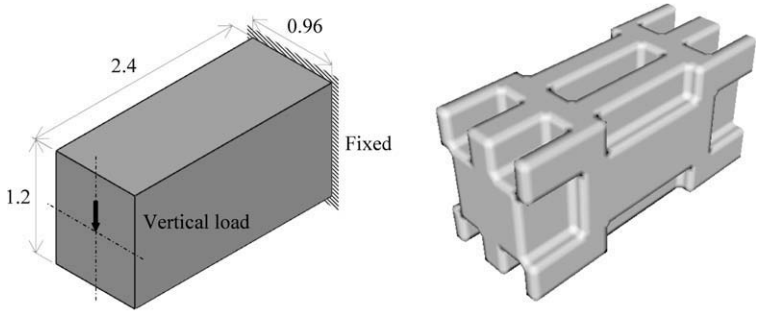


(a) A design domain (b) An initial shape

**Fig. 13.** A design domain and an initial shape for the 3D cantilever example.

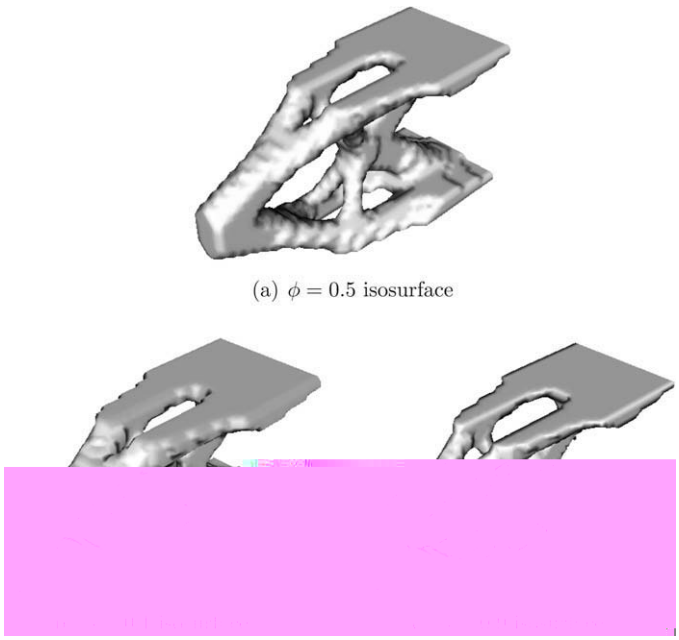

(a) $\phi = 0.5$ isosurface

**Fig. 14.** Optimal configurations of the 3D cantilever example.

### 5.4. Perimeter control

As discussed in Section 2, when the total volume of the phase field function is fixed in a closed domain composed of two phases, the total free energy minimization problem of the domain represented by Eq. (5) can be regarded as a perimeter minimization problem for each phase. That is, the evolutional equation derived from the free energy minimization problem can contain the perimeter control effect if the total volume of the phase field function is fixed. This can be applied to our method since the total volume of phase field function is constrained, and numerical examples show that perimeter control can be achieved by our method. A simple bridge optimization example shown in Fig. 15 is used here. The design domain is a $2 \times 1$ rectangle with fixed boundary conditions on the left and right lower edges and a vertical unit point load on the center of the bottom. The domain is discretized with a $200 \times 100$ rectangular mesh, and the objective function is formulated as the combination of the compliance and total volume of the structure. The coefficient $\kappa$ of the diffusion term in Eq. (41) is set to be either $\kappa = 7.5 \times 10^{-6}$ or $\kappa = 1 \times 10^{-5}$, while the Lagrange multiplier is updated to adjust the total volume of the optimal configuration to 0.6 during the optimization process.

Fig. 16 shows the optimal configurations obtained after 100 iterations for each choice of $\kappa$. The compliances of these optimal configurations are 22.4 and 23.3, respectively. We can see that the higher value of $\kappa$ yields an optimal configuration with fewer holes, that is, lower perimeter, even though they have the same initial shape.

### 5.5. Application to a compliant mechanism design problem and an eigenfrequency maximization problem

To confirm the versatility of our method, we now apply it to two other optimization problems, a compliant mechanism design problem [58,59] and an eigenfrequency maximization problem [68,69].

The examples of compliant mechanism optimization are typical benchmark problems, a force inverter and a gripper design problem given in [5]. The design domain of the force inverter problem is shown in Fig. 17. The design domain is a $2 \times 1$

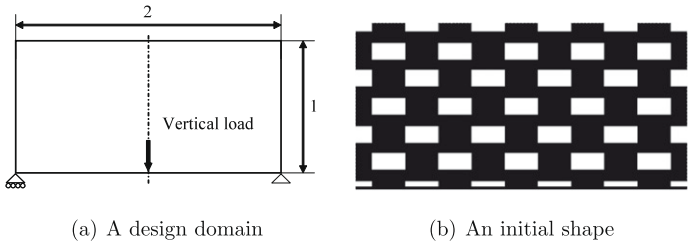


**Fig. 15.** A design domain and an initial shape for the bridge example.


**Fig. 16.** Optimal configurations of the bridge example with the different values of the coefficient of the diffusion term.

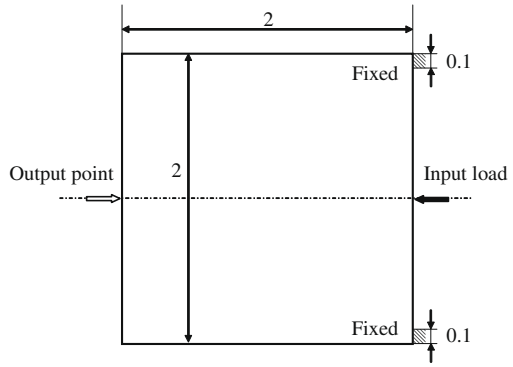


**Fig. 17.** A design domain for the inverter problem.

rectangle, with an input point and an output point on the center right and the center left of the domain, respectively. A horizontal unit point load is applied to the input point and the displacement of the output point is evaluated. The objective function is formulated as the combination of the least square error in Eq. (22) with $\alpha = 2$ and total volume of the structure. The coefficient function $c(\boldsymbol{x})$ is set to 1 at the output point and 0 elsewhere in the domain. The target displacement $\boldsymbol{u}_0$ is set to $(100, 0)$ at the output point. The characteristic of the objective function differs from that in the compliance problem in that the adjoint equation must be solved to calculate the derivative. The domain is discretized with a $200 \times 100$ rectangular mesh. The Lagrange multiplier is updated to adjust the total volume of the optimal configuration to 0.6 during the optimization process.We set $\kappa = 1 \times 10^{-5}$ in Eq. (41). Fig. 18 shows the optimal configuration and the deformed shape obtained after 100 iterations.

The design domain of the gripper problem is shown in Fig. 19. The black area is set as a non-design domain. A horizontal unit force is applied to the input point and the displacement of the output point is evaluated. In the objective function, $c(\boldsymbol{x})$ is set to 1 at the output point and 0 elsewhere. The target displacement is set to $(0, -100)$ at the output point. The domain is discretized with a $200 \times 100$ rectangular mesh, All parameters are set to the same as in the inverter example. Fig. 20 shows the optimal configuration after 100 iterations and the deformed shape.

The convergence history for both of these examples is shown in Fig. 21. The optimal configurations and convergence history show that our method is effective for compliant mechanism problems. Moreover, an additional advantage of our method is that there are no hinges in our optimal configuration, because the mean curvature motion of the diffuse interface is contained in the phase field method and a discontinuous structure is penalized implicitly.

We also perform the optimization of a 3D gripper mechanism. As with the 2D case, a load is applied to the center of the right side of the domain, and the upper and lower sides are fixed as shown in Fig. 22(a). The domain is discretized with a $60 \times 24 \times 60$ cubic mesh and the value of the Lagrange multiplier $\zeta$ is updated to adjust the total volume of the optimal configuration to 0.55 (10% of total volume) during the optimization process. Only one quarter of the domain is computed due to symmetry. We set the initial shape as shown in Fig. 22(b), and $\kappa = 1.5 \times 10^{-4}$ in Eq. (41). The $\phi = 0.5$ isosurface of the optimal configuration obtained after 50 iterations is shown in Fig. 23. This example shows that our method works well in 3D mechanism examples.

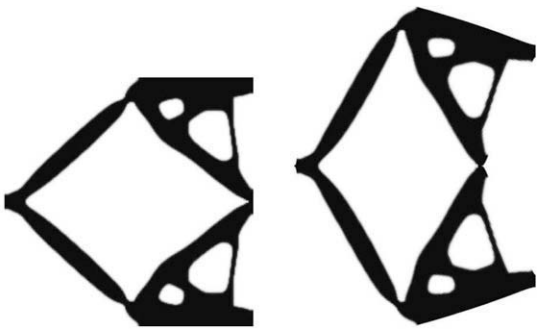

(a) An optimal configuration (b) The deformed shape

**Fig. 18.** An optimal result and the deformed shape of the inverter problem.

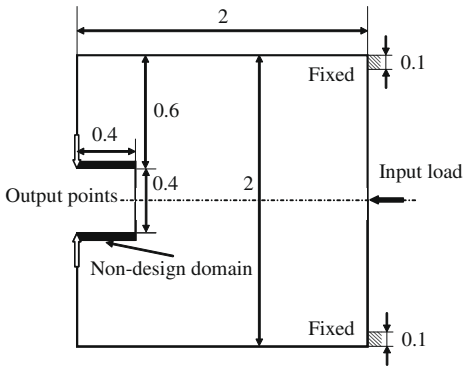


**Fig. 19.** A design domain for the gripper problem.

Finally, we come to the eigenfrequency maximization problems. We set the cantilever-like design domain with a point mass of 100 in the center of the right side as shown in Fig. 24. To avoid the localized mode of the ersatz material domain, the interpolation functions for material properties in Eq. (42) are set as follows, based on [69]:

$$k(\phi) = \begin{cases} \phi^3 & \text{for } 0.1 \leqslant \phi < 1 \\ \min(\phi/100, 10^{-5}) & \text{for } 0 < \phi < 0.1 \end{cases}, \quad m(\phi) = \min(\phi, 10^{-3}). \tag{48}$$

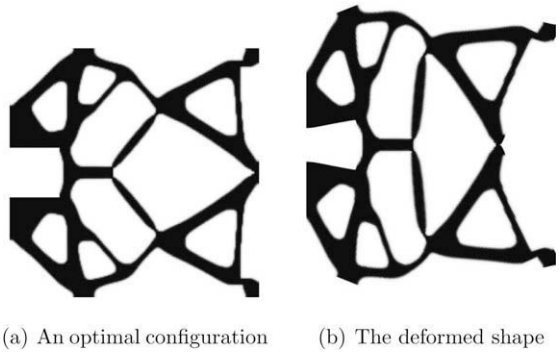


**Fig. 20.** An optimal result and the deformed shape of the gripper problem.

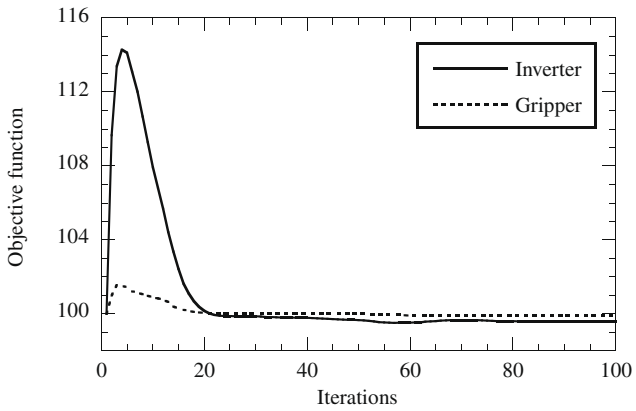


**Fig. 21.** The convergence history of the objective function of the mechanism example.

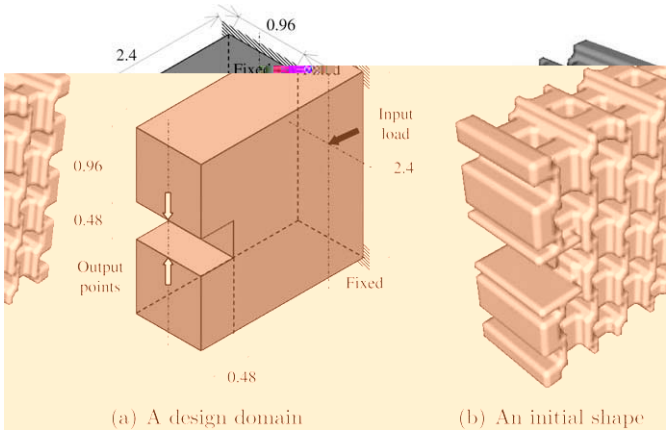


**Fig. 22.** A design domain and an initial shape for the 3D gripper example.

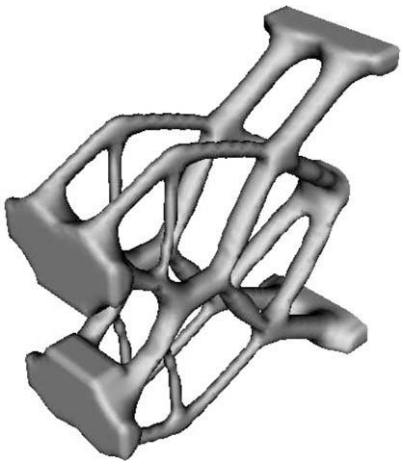

**Fig. 23.** An optimal result of the 3D gripper problem.

The objective function is formulated as the sum of the eigenvalues in Eq. (25) and the total volume of the structure. The domain is discretized with a $200 \times 100$ rectangular mesh, and the Lagrange multiplier is updated to adjust the total volume of the optimal configuration to 0.8, while we use $\kappa = 1 \times 10^{-5}$ in Eq. (41).

Fig. 25 shows the optimal configuration and the first eigenmode shape in the case that the first eigenvalue is maximized. Since the first mode is the vertical movement of the concentrated mass, the optimal configuration has a similar shape to the previous cantilever stiffness maximization problem.

Fig. 26 shows the optimal configuration and the second mode shape in the case that the first and the second eigenvalues are maximized simultaneously. The weight coefficients of both eigenvalues in Eq. (25) are set to 0.5. Due to the effect of the second eigenmode with horizontal displacement, the optimal configuration is quite different from the previous case. Fig. 27 shows the convergence history of eigenfrequencies in each case, from which the maximization of the target eigenfrequency can be observed.

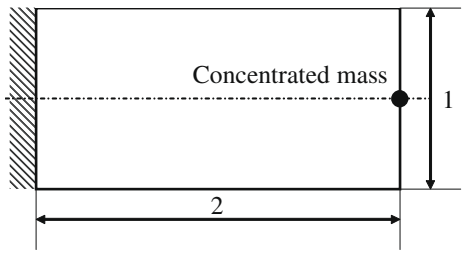


**Fig. 24.** A design domain for the eigenfrequency maximization problem.

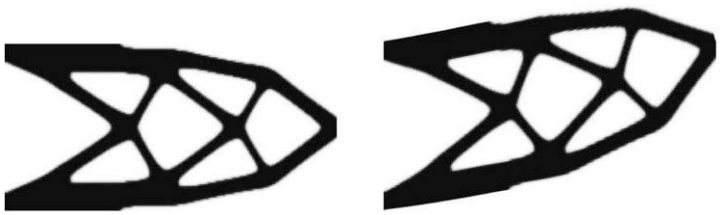

(a) An optimal configuration (b) The deformed shape of the lowest mode

**Fig. 25.** An optimal configuration and the deformed mode shape of the eigenfrequency maximization problem.

(a) An optimal configuration (b) The deformed shape of the second lowest mode

**Fig. 26.** An optimal configuration and the deformed mode shape of the eigenfrequency maximization problem.

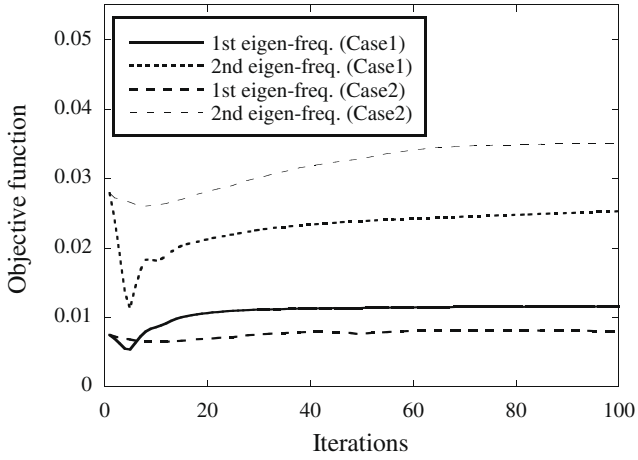


**Fig. 27.** The convergence history of the eigenfrequencies (Case 1: only the lowest eigenfrequency is maximized; Case 2: the two lowest eigenfrequencies are maximized).

## 6. Conclusion

We have proposed a new method for structural shape and topology optimization based on the phase field method. Although our method achieves the same functional capabilities with perimeter control as the level set method, our method has an advantage in terms of simplicity, since we do not require extra re-initializing operations of the domain representing function. Our method is especially effective in the case of perimeter constrained problems. Since the perimeter control effect is included implicitly as a characteristic of the phase field method, our method requires no additional calculations such as the calculation of curvatures. However, the perimeter control effect (the mean curvature motion of the diffuse interface) cannot be canceled completely although its effect can be controlled by varying $\kappa$. Alternatively, the mean curvature motion cancellation method can be applied here [35,39].

Another drawback is the dependence on the initial shape, which as discussed in [16], is typical of structural optimization methods based on boundary variation. To resolve this fundamental problem, the bubble method or topological derivative [62,63] can be introduced to our method as in the numerical examples. Another option is to generate an initial shape by topology optimization. In that case, our method has an advantage in terms of implementation, since our domain representation is quite similar to the density function used topology optimization, even though their physical meanings are completely different.

## Acknowledgment

We would like to thank Ryo Kobayashi for his valuable comments and advice on the phase field method.

## Appendix A. Sensitivity analysis

The derivatives of the objective functions with respect to the phase field function are based on [3]. We use the word "derivative" in the sense of the Fréchet derivative. First, the general objective function is defined as

$$J(\phi) = \int_D j(\boldsymbol{u})dx + \int_{\partial D_N} l(\boldsymbol{u})ds. \tag{49}$$

The derivative of this function in the direction $\theta$ is then

$$\langle J'(\phi), \theta\rangle = \int_D j'(\boldsymbol{u})\langle \boldsymbol{u}'(\phi), \theta\rangle dx + \int_{\partial D_N} l'(\boldsymbol{u})\langle \boldsymbol{u}'(\phi), \theta\rangle ds = \int_D j'(\boldsymbol{u})\boldsymbol{v}dx + \int_{\partial D_N} l'(\boldsymbol{u})\boldsymbol{v}ds, \tag{50}$$

where $\boldsymbol{v} = \langle \boldsymbol{u}'(\phi), \theta\rangle$. Using the state equation of the linear elasticity problem from Eq. (18), the Lagrangian is

$$L(\phi, \boldsymbol{u}, \boldsymbol{p}) = \int_D j(\boldsymbol{u})dx + \int_{\partial D_N} l(\boldsymbol{u})ds + \int_D \boldsymbol{A}^*(\phi)\boldsymbol{e}(\boldsymbol{u}) : \boldsymbol{e}(\boldsymbol{p})dx - \int_{\partial D_N} \boldsymbol{g}\cdot\boldsymbol{p}ds, \tag{51}$$

where $\boldsymbol{u}$ is the displacement and $\boldsymbol{p}$ is the adjoint state. Using this, the derivative can be expressed as

$$\langle J'(\phi), \theta\rangle = \left\langle \frac{\partial L}{\partial \phi}(\phi, \boldsymbol{u}, \boldsymbol{p}), \theta \right\rangle + \left\langle \frac{\partial L}{\partial \boldsymbol{u}}(\phi, \boldsymbol{u}, \boldsymbol{p}), \langle \boldsymbol{u}'(\phi), \theta\rangle \right\rangle. \tag{52}$$

Consider the case where the second term is zero. Replacing $\langle \boldsymbol{u}'(\phi), \theta\rangle$ with $\boldsymbol{v}$, the second term is

$$\left\langle \frac{\partial L}{\partial \boldsymbol{u}}(\phi, \boldsymbol{u}, \boldsymbol{p}), \boldsymbol{v} \right\rangle = \int_D j'(\boldsymbol{u})\boldsymbol{v}dx + \int_{\partial D_N} l'(\boldsymbol{u})\boldsymbol{v}ds + \int_D \boldsymbol{A}^*(\phi)\boldsymbol{e}(\boldsymbol{v}) : \boldsymbol{e}(\boldsymbol{p})dx = 0. \tag{53}$$

In the case that the adjoint state $\boldsymbol{p}$ satisfies the above adjoint equation, the second term of Eq. (52) can be ignored. On the other hand, the derivative of Eq. (18) with respect to $\phi$ in the direction $\theta$ is

$$\int_D \langle \boldsymbol{A}^{*\prime}(\phi), \theta\rangle \boldsymbol{e}(\boldsymbol{u}) : \boldsymbol{e}(\boldsymbol{p})dx + \int_D \boldsymbol{A}^*(\phi)\boldsymbol{e}(\langle \boldsymbol{u}'(\phi), \theta\rangle) : \boldsymbol{e}(\boldsymbol{p})dx = \int_D \boldsymbol{A}^{*\prime}(\phi)\boldsymbol{e}(\boldsymbol{u}) : \boldsymbol{e}(\boldsymbol{p})\theta dx + \int_D \boldsymbol{A}^*(\phi)\boldsymbol{e}(\boldsymbol{v}) : \boldsymbol{e}(\boldsymbol{p})dx = 0. \tag{54}$$

If we compare this with Eqs. (53) and (54), the following can be obtained:

$$\int_D j'(\boldsymbol{u})\boldsymbol{v}dx + \int_{\partial D_N} l'(\boldsymbol{u})\boldsymbol{v}ds = \int_D \boldsymbol{A}^{*\prime}(\phi)\boldsymbol{e}(\boldsymbol{u}) : \boldsymbol{e}(\boldsymbol{p})\theta dx. \tag{55}$$

Substituting Eq. (55) into Eq. (50), the derivative of the objective function is

$$J'(\phi) = \boldsymbol{A}^{*\prime}(\phi)\boldsymbol{e}(\boldsymbol{u}) : \boldsymbol{e}(\boldsymbol{p}). \tag{56}$$

We now apply the above equation to Eqs. (21) and (22). In the case of the compliance in Eq. (21), Eq. (53) becomes equal to the state equation by replacing $\boldsymbol{p}$ with $-\boldsymbol{u}$. That is, this problem is self-adjoint and the derivative of the objective function in Eq. (32) can be calculated directly from Eq. (56). In the case of the least square error compared with the target displacement, the adjoint equation in Eq. (34) is obtained by substituting the objective function from Eq. (22) into Eq. (53).

We also consider the vibration problem whose objective function is $k$th eigenvalue. That is,

$$J(\phi) = \lambda_k. \tag{57}$$

Using the state equation from Eq. (24), the Lagrangian is

$$L(\phi, \boldsymbol{u}_k, \boldsymbol{p}) = \lambda_k + \int_D \boldsymbol{A}^*(\phi)\boldsymbol{e}(\boldsymbol{u}_k) : \boldsymbol{e}(\boldsymbol{p})dx - \lambda_k \int_D \rho^*(\phi)\boldsymbol{u}_k\cdot\boldsymbol{p}dx, \tag{58}$$

where $\boldsymbol{u}_k$ is the normalized $k$th eigenmode vector. That is $\int_D \rho^*(\phi)|\boldsymbol{u}_k|^2 dx = 1$. Using the Lagrangian, the derivative of this function may be given as

$$\langle J'(\phi), \theta\rangle = \left\langle \frac{\partial L}{\partial \phi}(\phi, \boldsymbol{u}_k, \boldsymbol{p}), \theta \right\rangle + \left\langle \frac{\partial L}{\partial \boldsymbol{u}_k}(\phi, \boldsymbol{u}_k, \boldsymbol{p}), \langle \boldsymbol{u}_k'(\phi), \theta\rangle \right\rangle. \tag{59}$$

The second term of Eq. (59) is

$$\left\langle \frac{\partial L}{\partial \phi}(\phi, \boldsymbol{u}_k, \boldsymbol{p}), \boldsymbol{v}_k \right\rangle = \langle \lambda_k'(\boldsymbol{u}_k), \boldsymbol{v}_k\rangle \left(1 - \int_D \rho^*(\phi)\boldsymbol{u}_k\cdot\boldsymbol{p}dx\right) - \left(\int_D \boldsymbol{A}^*(\phi)\boldsymbol{e}(\boldsymbol{v}_k) : \boldsymbol{e}(\boldsymbol{p})dx - \lambda_k \int_D \rho^*(\phi)\boldsymbol{v}_k\cdot\boldsymbol{p}dx\right), \tag{60}$$

where $\boldsymbol{v}_k = \langle \boldsymbol{u}_k'(\phi), \theta\rangle$. In the case that $\boldsymbol{u}_k = \boldsymbol{v}_k$, the right-hand side of the above equation becomes zero. Thus this problem is also self-adjoint. Moreover, replacing the arbitrary test function $\boldsymbol{p}$ by $\boldsymbol{u}_k$, the first term can be eliminated. The derivative of Eq. (24) with respect to $\phi$ in the direction $\theta$ is

$$\begin{aligned}\int_D \langle \boldsymbol{A}^{*\prime}(\phi), \theta\rangle \boldsymbol{e}(\boldsymbol{u}_k) : \boldsymbol{e}(\boldsymbol{p})dx + \int_D \boldsymbol{A}^*(\phi)\boldsymbol{e}(\boldsymbol{v}_k) : \boldsymbol{e}(\boldsymbol{p})dx \\ = \langle \lambda_k'(\phi), \theta\rangle \int_D \rho^*(\phi)\boldsymbol{u}_k\cdot\boldsymbol{p}dx + \lambda_k \int_D \langle \rho^{*\prime}(\phi), \theta\rangle \boldsymbol{u}_k\cdot\boldsymbol{p}dx + \lambda_k \int_D \rho^*(\phi)\boldsymbol{v}_k\cdot\boldsymbol{p}dx,\end{aligned} \tag{61}$$

where $\boldsymbol{v}_k = \langle \boldsymbol{u}_k'(\phi), \theta\rangle$. Replacing both $\boldsymbol{v}_k$ and $\boldsymbol{p}$ by $\boldsymbol{u}_k$, the equation becomes:

$$\langle \lambda_k'(\phi), \theta \rangle = \int_D \langle \boldsymbol{A}^{*\prime}(\phi), \theta \rangle \boldsymbol{e}(\boldsymbol{u}_k) : \boldsymbol{e}(\boldsymbol{p}) dx - \lambda_k \int_D \langle \rho^{*\prime}(\phi), \theta \rangle |\boldsymbol{u}_k|^2 dx = \int_D (\boldsymbol{A}^{*\prime}(\phi) \boldsymbol{e}(\boldsymbol{u}_k) : \boldsymbol{e}(\boldsymbol{u}_k) - \lambda_k \rho^{*\prime}(\phi) |\boldsymbol{u}_k|^2) \theta dx. \tag{62}$$

Thus, the sensitivity of the $k$th eigenvalue is

$$\lambda_k'(\phi) = \boldsymbol{A}^{*\prime}(\phi) \boldsymbol{e}(\boldsymbol{u}_k) : \boldsymbol{e}(\boldsymbol{u}_k) - \lambda_k \rho^{*\prime}(\phi) |\boldsymbol{u}_k|^2. \tag{63}$$

## Appendix B. Discretization of the reaction term

We now discuss the effect of the reaction term on the convergence of the phase field function in the Allen–Cahn equation (41). If the equation is discretized by an explicit scheme, the time step $\Delta t$ is restricted by requiring stable convergence of the reaction term, in addition to the CFL condition for the diffusion term. To confirm this, we perform some simple numerical tests. Let us consider the following ordinary differential equation:

$$\frac{du}{dt} = -f'(u) = -\left(\frac{1}{4} w'(u) + d g'(u)\right) = u(1-u)\left\{u - \frac{1}{2} - 30d(1-u)u\right\}. \tag{64}$$

The above equation is simplified from Eq. (41) by ignoring the diffusion term, replacing the function $\phi$ by a variable $u$, and simplifying the sensitivity coefficient $\eta \frac{J'(\phi_{t_1})}{\|J'(\phi_{t_1})\|}$ to a coefficient $d$. The equation is discretized by an explicit scheme as follows:

$$\frac{u^{n+1} + u^n}{\Delta t} = u^n(1-u^n)\left\{u^n - \frac{1}{2} - 30d(1-u^n)u^n\right\}. \tag{65}$$

We start the numerical tests by solving the above equation with the initial value $u^0 = 0.5$ for the $\Delta t = 0.01$, 0.1 and 1, and $d = 0.1$, 1, 10, $-0.1$, $-1$ and $-10$. If $d$ is positive, the analytical result is $u = 0$; if not, then $u = 1$. Table 1 shows the value of $u$ at times $t = 0$, 2, 4, 6, 8, and 10. We can clearly see that $u$ diverges in Eq. (65) if $d$ and $\Delta t$ are large. A large value of $\Delta t$ allows $u$ to exceed its theoretical bound of $0 \leqslant \phi \leqslant 1$. Moreover, a large value of $d$ causes the function $g(u)$ to dominate $f(u)$, which rapidly decreases with $u$ if $u < 0$. The same can be said if $u > 1$, since the derivative of $f(u)$ is also steep when $u < 0$, and so the case $u > 1$ tends to the case $u < 0$. To obtain ideal results from Eq. (64) with $u = 0$ or $u = 1$, it is important to bound the variable $u$ in the interval $0 \leqslant u \leqslant 1$. The easiest way to do this is to force the variable $u^{n+1}$ into $0 \leqslant u \leqslant 1$ at each iteration. However, in our research, the more sophisticated semi-implicit scheme [38] is used. In this method, the equation is discretized as follows:

$$\frac{u^{n+1} + u^n}{\Delta t} = \begin{cases} u^{n+1}(1-u^n) r(u) & \text{for } r(u^n) \leqslant 0, \\ u^n(1-u^{n+1}) r(u) & \text{for } r(u^n) > 0, \end{cases} \tag{66}$$

where

$$r(u^n) = u^n - \frac{1}{2} - 30d(1-u^n)u^n. \tag{67}$$

**Table 1**
Results of a test problem solved by an explicit scheme.

| $t$ | $d = 0.1$ | | | $d = 1$ | | | $d = 10$ | | |
|---|---|---|---|---|---|---|---|---|---|
| | $\Delta t = 0.01$ | $\Delta t = 0.1$ | $\Delta t = 1$ | $\Delta t = 0.01$ | $\Delta t = 0.1$ | $\Delta t = 1$ | $\Delta t = 0.01$ | $\Delta t = 0.1$ | $\Delta t = 1$ |
| 0 | 0.5000 | 0.5000 | 0.5000 | 0.5000 | 0.5000 | 0.5000 | 0.5000 | 0.5000 | 0.5000 |
| 2 | 0.1668 | 0.1640 | 0.1337 | 0.0114 | 0.0092 | −315.18 | 0.0010 | – | $-3.7 \times 10^{7}$ |
| 4 | 0.0504 | 0.0480 | 0.0223 | 0.0030 | 0.0024 | $-2.4 \times 10^{47}$ | 0.0003 | – | $-3.0 \times 10^{133}$ |
| 6 | 0.0170 | 0.0158 | 0.0051 | 0.0010 | 0.0008 | – | 0.0001 | – | – |
| 8 | 0.0061 | 0.0055 | 0.0012 | 0.0003 | 0.0003 | – | 0.0000 | – | – |
| 10 | 0.0022 | 0.0020 | 0.0003 | 0.0001 | 0.0001 | – | 0.0000 | – | – |
| | $d = -0.1$ | | | $d = -1$ | | | $d = -10$ | | |
| 0 | 0.5000 | 0.5000 | 0.5000 | 0.5000 | 0.5000 | 0.5000 | 0.5000 | 0.5000 | 0.5000 |
| 2 | 0.8332 | 0.8360 | 0.8663 | 0.9886 | 0.9908 | 316.18 | 0.9990 | – | $-3.7 \times 10^{7}$ |
| 4 | 0.9496 | 0.9520 | 0.9777 | 0.9970 | 0.9976 | $2.4 \times 10^{47}$ | 0.9997 | – | $-3.0 \times 10^{133}$ |
| 6 | 0.9830 | 0.9842 | 0.9949 | 0.9990 | 0.9992 | – | 0.9999 | – | – |
| 8 | 0.9939 | 0.9945 | 0.9988 | 0.9997 | 0.9997 | – | 1.0000 | – | – |
| 10 | 0.9978 | 0.9980 | 0.9997 | 0.9999 | 0.9999 | – | 1.0000 | – | – |

– indicates overflow.

**Table 2**
Results of the test problem solved by a semi-implicit scheme.

| $t$ | $d = 0.1$ | | | $d = 1$ | | | $d = 10$ | | |
|---|---|---|---|---|---|---|---|---|---|
| | $\Delta t = 0.01$ | $\Delta t = 0.1$ | $\Delta t = 1$ | $\Delta t = 0.01$ | $\Delta t = 0.1$ | $\Delta t = 1$ | $\Delta t = 0.01$ | $\Delta t = 0.1$ | $\Delta t = 1$ |
| 0 | 0.5000 | 0.5000 | 0.5000 | 0.5000 | 0.5000 | 0.5000 | 0.5000 | 0.5000 | 0.5000 |
| 2 | 0.1679 | 0.1753 | 0.2379 | 0.0118 | 0.0128 | 0.0271 | 0.0010 | 0.0011 | 0.0025 |
| 4 | 0.0511 | 0.0546 | 0.0909 | 0.0031 | 0.0033 | 0.0066 | 0.0003 | 0.0003 | 0.0006 |
| 6 | 0.0173 | 0.0189 | 0.0362 | 0.0010 | 0.0011 | 0.0024 | 0.0001 | 0.0001 | 0.0002 |
| 8 | 0.0062 | 0.0069 | 0.0153 | 0.0004 | 0.0004 | 0.0010 | 0.0000 | 0.0000 | 0.0001 |
| 10 | 0.0023 | 0.0026 | 0.0066 | 0.0001 | 0.0002 | 0.0004 | 0.0000 | 0.0000 | 0.0000 |
| | $d = -0.1$ | | | $d = -1$ | | | $d = -10$ | | |
| 0 | 0.5000 | 0.5000 | 0.5000 | 0.5000 | 0.5000 | 0.5000 | 0.5000 | 0.5000 | 0.5000 |
| 2 | 0.8321 | 0.8247 | 0.7621 | 0.9882 | 0.9872 | 0.9729 | 0.9990 | 0.9989 | 0.9975 |
| 4 | 0.9489 | 0.9454 | 0.9091 | 0.9969 | 0.9967 | 0.9934 | 0.9997 | 0.9997 | 0.9994 |
| 6 | 0.9827 | 0.9811 | 0.9638 | 0.9990 | 0.9989 | 0.9976 | 0.9999 | 0.9999 | 0.9998 |
| 8 | 0.9938 | 0.9931 | 0.9847 | 0.9996 | 0.9996 | 0.9990 | 1.0000 | 1.0000 | 0.9999 |
| 10 | 0.9977 | 0.9974 | 0.9934 | 0.9999 | 0.9998 | 0.9996 | 1.0000 | 1.0000 | 1.0000 |

Finally the update value $u^{n+1}$ is obtained by:

$$u^{n+1} = \begin{cases} \frac{u^n}{1-\Delta t(1-u^n)r(u^n)} & \text{for } r(u^n) \leqslant 0, \\ \frac{u^n(1+\Delta t r(u^n))}{1+\Delta t u^n r(u^n)} & \text{for } r(u^n) > 0. \end{cases} \tag{68}$$

We can see that $u^{n+1}$ is non-negative in both cases if $0 \leqslant u^n \leqslant 1$. Whether $u^{n+1}$ satisfies the bound $u \leqslant 1$ is also easily checked by calculating $1 - u^{n+1}$ from Eq. (68):

$$1 - u^{n+1} = \begin{cases} \frac{1-u^n-\Delta t(1-u^n)r(u^n)}{1-\Delta t(1-u^n)r(u^n)} & \text{for } r(u^n) \leqslant 0, \\ \frac{1-u^n}{1+\Delta t u^n r(u^n)} & \text{for } r(u^n) > 0. \end{cases} \tag{69}$$

$u^{n+1}$ is again clearly non-negative in both cases. Thus, the discretization given in Eq. (66) is bounded by $0 \leqslant u \leqslant 1$ independent of the time step $\Delta t$. Table 2 shows the results of the same test solved by the semi-implicit scheme, which confirms stable convergence for any $\Delta t$ and $d$.

## References


[1] A.G.M. Michell, The limits of economy of material in frame structures, Lond. Edinb. Dubl. Philos. Mag. Ser. 68 (47) (1904) 589–597.
[2] G. Allaire, Shape Optimization by the Homogenization Method, Springer-Verlag, New York, 2001.
[3] G. Allaire, Conception Optimale De Structures, Springer-Verlag, Berlin, 2007.
[4] N.V. Banichuk, Introduction to Optimization of Structures, Springer-Verlag, New York, 1990.
[5] M.P. Bendsøe, O. Sigmund, Topology Optimization: Theory, Methods, and Applications, Springer-Verlag, Berlin, 2003.
[6] A. Cherkaev, Variational Methods for Structural Optimization, Springer, New York, 2000.
[7] J. Haslinger, R.A.E. Mäkinen, Introduction to Shape Optimization: Theory, Approximation, and Computation, SIAM, Philadelphia, 2003.
[8] W.S. Hemp, Optimum Structures, Clarendon Press, Oxford, 1973.
[9] U. Kirsch, Optimum Structural Design, McGraw-Hill Education, New York, 1981.
[10] B. Mohammadi, O. Pironneau, Applied Shape Optimization for Fluids, Oxford University Press, Oxford, 2001.
[11] O. Pironneau, Optimal Shape Design for Elliptic Systems, Springer-Verlag, New York, 1984.
[12] G.I.N. Rozvany, Structural Design via Optimality Criteria, Kluwer Academic Publishers, Dordrecht, 1989.
[13] J. Sokołowski, J.P. Zolesio, Introduction to Shape Optimization: Shape Sensitivity Analysis, Springer-Verlag, Berlin, 1992.
[14] M.P. Bendsøe, N. Kikuchi, Generating optimal topologies in structural design using a homogenization method, Comput. Meth. Appl. Mech. Eng. 71 (2) (1988) 197–224.
[15] B. Bourdin, Filters in topology optimization, Int. J. Numer. Meth. Eng. 50 (9) (2001) 2143–2158.
[16] G. Allaire, F. Jouve, A. Toader, Structural optimization using sensitivity analysis and a level-set method, J. Comput. Phys. 194 (1) (2004) 363–393.
[17] S.J. Osher, F. Santosa, Level set methods for optimization problems involving geometry and constraints. I. Frequencies of a two-density inhomogeneous drum, J. Comput. Phys. 171 (2001) 272–288.
[18] J.A. Sethian, A. Wiegmann, Structural boundary design via level set and immersed interface methods, J. Comput. Phys. 163 (2) (2000) 489–528.
[19] M.Y. Wang, X. Wang, D. Guo, A level set method for structural topology optimization, Comput. Meth. Appl. Mech. Eng. 192 (1–2) (2003) 227–246.
[20] S. Osher, J.A. Sethian, Fronts propagating with curvature-dependent speed: algorithms based on Hamilton–Jacobi formulations, J. Comput. Phys. 79 (1988) 12–49.
[21] Y.G. Chen, Y. Giga, S. Goto, Uniqueness and existence of viscosity solutions of generalized mean curvature flow equations, J. Diff. Geom. 33 (3) (1991) 749–786.
[22] L.C. Evans, J. Spruck, Motion of level sets by mean curvature. I, J. Diff. Geom. 33 (3) (1991) 635–681.
[23] Y. Giga, Surface Evolution Equations: A Level Set Approach, Birkhäuser, Basel, 2006.
[24] D.L. Chopp, Computing minimal surfaces via level set curvature flow, J. Comput. Phys. 106 (1993) 77–91.
[25] J.A. Sethian, Level Set Methods and Fast Marching Methods, Cambridge University Press, New York, 1999.
[26] M. Sussman, P. Smereka, S. Osher, A level set approach for computing solutions to incompressible two-phase flow, J. Comput. Phys. 114 (1994) 146–159.
[27] S. Osher, R. Fedkiw, Level Set Methods and Dynamic Implicit Surfaces, Springer-Verlag, New York, 2002.
[28] J.W. Cahn, J.E. Hilliard, Free energy of a nonuniform system. I. Interfacial free energy, J. Chem. Phys. 28 (1958) 258–267.

[29] S.M. Allen, J.W. Cahn, A microscopic theory for antiphase boundary motion and its application to antiphase domain coarsening, Acta Metall. 27 (1979) 1085–1095.
[30] G. Caginalp, An analysis of a phase field model of a free boundary, Arch. Rat. Mech. Anal. 92 (3) (1986) 205–245.
[31] J.B. Collins, H. Levine, Diffuse interface model of diffusion-limited crystal growth, Phys. Rev. B 31 (9) (1985) 6119–6122.
[32] G. Fix, Phase field models for free boundary problems, in: A. Fasano, M. Primicerio (Eds.), Free Boundary Problems, Theory and Application, Pitman, New York, 1983, pp. 580–589.
[33] R. Kobayashi, Modeling and numerical simulations of dendritic crystal growth, Physica D 63 (3–4) (1993) 410–423.
[34] S. Wang, R. Sekerka, A. Wheeler, B. Murray, S. Coriell, R. Braun, G. McFadden, Thermodynamically-consistent phase-field models for solidification, Physica D 69 (1–2) (1993) 189–200.
[35] R. Folch, J. Casademunt, A. Hernández-Machado, L. Ramírez-Piscina, Phase-field model for hele-shaw flows with arbitrary viscosity contrast. I. Theoretical approach, Phys. Rev. E 60 (2) (1999) 1724–1733.
[36] I.S. Aranson, V.A. Kalatsky, V.M. Vinokur, Continuum field description of crack propagation, Phys. Rev. Lett. 85 (1) (2000) 118–121.
[37] R. Kobayashi, J.A. Warren, W. Craig Carter, A continuum model of grain boundaries, Physica D 140 (1–2) (2000) 141–150.
[38] J.A. Warren, R. Kobayashi, A.E. Lobkovsky, W. Craig Carter, Extending phase field models of solidification to polycrystalline materials, Acta Mater. 51 (20) (2003) 6035–6058.
[39] Y. Sun, C. Beckermann, Sharp interface tracking using the phase-field equation, J. Comput. Phys. 220 (2) (2007) 626–653.
[40] W.J. Boettinger, J.A. Warren, C. Beckermann, A. Karma, Phase-field simulation of solidification, Annu. Rev. Mater. Res. 32 (2002) 163–194.
[41] L.Q. Chen, Phase-field models for microstructure evolution, Annu. Rev. Mater. Res. 32 (2002) 113–140.
[42] G.B. Macfadden, Phase-field models of solidification, Contemp. Math. 306 (2002) 107–145.
[43] B. Bourdin, A. Chambolle, Design-dependent loads in topology optimization, ESAIM Contr. Optim. Calc. Var. 9 (2003) 19–48.
[44] B. Bourdin, A. Chambolle, The phase-field method in optimal design, in: IUTAM Symposium on Topological Design Optimization of Structures, Machines and Materials, 2006, pp. 207–215.
[45] L. Ambrosio, G. Buttazzo, An optimal design problem with perimeter penalization, Calc. Var. 1 (1993) 55–69.
[46] R.B. Haber, C.S. Jog, M.P. Bendsøe, A new approach to variable-topology shape design using a constraint on perimeter, Struct. Optim. 11 (1) (1996) 1–12.
[47] M. Burger, R. Stainko, Phase-field relaxation of topology optimization with local stress constraints, SIAM J. Contr. Optim. 45 (4) (2006) 1447–1466.
[48] M.Y. Wang, S. Zhou, Phase field: a variational method for structural topology optimization, Comput. Model. Eng. Sci. 6 (6) (2004) 547–566.
[49] S. Zhou, M. Wang, Multimaterial structural topology optimization with a generalized Cahn–Hilliard model of multiphase transition, Struct. Multidisc. Optim. 33 (2) (2007) 89–111.
[50] S. Zhou, M. Wang, C. Source, 3D multi-material structural topology optimization with the generalized Cahn–Hilliard equations, Comput. Model. Eng. Sci. 16 (2) (2006) 83–102.
[51] G. Barles, H.M. Soner, P.E. Souganidis, Front propagation and phase field theory, SIAM J. Contr. Optim. 31 (1993) 439–469.
[52] P. Fife, Dynamics of Internal Layers and Diffusive Interfaces, SIAM, Philadelphia, 1988.
[53] J. Rubinstein, P. Sternberg, J.B. Keller, Fast reaction, slow diffusion, and curve shortening, SIAM J. Appl. Math. 49 (1989) 116–133.
[54] A. Braides, Gamma-convergence for Beginners, Oxford University Press, New York, 2002.
[55] L. Modica, The gradient theory of phase transitions and the minimal interface criterion, Arch. Rat. Mech. Anal. 98 (2) (1987) 123–142.
[56] M.P. Bendsøe, O. Sigmund, Material interpolation schemes in topology optimization, Arch. Appl. Mech. 69 (9) (1999) 635–654.
[57] L. Tartar, Remarks on optimal design problems, Calculus of Variations: Homogenization and Continuum Mechanics, Series on Adv. in Math. for Appl. Sci, vol. 18, World Scientific, Singapore, 1994.
[58] S. Nishiwaki, M. Frecker, S. Min, N. Kikuchi, Topology optimization of compliant mechanisms using the homogenization method, Int. J. Numer. Meth. Eng. 42 (1998) 535–559.
[59] O. Sigmund, On the design of compliant mechanisms using topology optimization, Mech. Struct. Mach. 25 (4) (1997) 493–524.
[60] R.J. Leveque, Finite Volume Methods for Hyperbolic Problems, Cambridge University Press, New York, 2002.
[61] G. Allaire, O. Pantz, Structural optimization with freefem++, Struct. Multidisc. Optim. 32 (3) (2006) 173–181.
[62] H.A. Eschenauer, V.V. Kobelev, A. Schumacher, Bubble method for topology and shape optimization of structures, Struct. Optim. 8 (1) (1994) 42–51.
[63] J. Sokołowski, A. Zochowski, On topological derivative in shape optimization, SIAM J. Contr. Optim. 37 (4) (1999) 1251–1272.
[64] J. Céa, S. Garreau, P. Guillaume, M. Masmoudi, The shape and topological optimizations connection, Comput. Meth. Appl. Mech. Eng. 188 (4) (2000) 713–726.
[65] S. Garreau, P. Guillaume, M. Masmoudi, The topological asymptotic for PDE systems: the elasticity case, SIAM J. Contr. Optim. 39 (6) (2001) 1756–1778.
[66] G. Allaire, F. de Gournay, F. Jouve, A. Toader, Structural optimization using topological and shape sensitivity via a level set method, Contr. Cybern. 34 (1) (2005) 59–80.
[67] L. He, C.Y. Kao, S. Osher, Incorporating topological derivatives into shape derivatives based level set methods, J. Comput. Phys. 225 (1) (2007) 891–909.
[68] Z.D. Ma, N. Kikuchi, H.C. Cheng, Topological design for vibrating structures, Comput. Meth. Appl. Mech. Eng. 121 (1–4) (1995) 259–280.
[69] N.L. Pedersen, Maximization of eigenvalues using topology optimization, Struct. Multidisc. Optim. 20 (1) (2000) 2–11.